Research Article | Vol. 26, No. 4 | 19 Feb 2018 | OPTICS EXPRESS 4204

Optics EXPRESS

Tuning the strain-induced resonance shift in silicon racetrack resonators by their orientation

CLAUDIO CASTELLAN,[1,*] ASTGHIK CHALYAN,[1,2] MATTIA MANCINELLI,[1,3] PIERRE GUILLEME,[1] MASSIMO BORGHI,[1] FEDERICO BOSIA,[4] NICOLA M. PUGNO,[5,6,7] MARTINO BERNARD,[8] MHER GHULINYAN,[8] GEORG PUCKER,[8] AND LORENZO PAVESI[1]

[1]*Nanoscience Laboratory, Department of Physics, University of Trento, via Sommarive 14, 38123 Trento, Italy*
[2]*Russian-Armenian (Slavonic) University, H. Emin 123, 0051 Yerevan, Armenia*
[3]*Research Programs, SM Optics s.r.l., via John Fitzgerald Kennedy 2, 20871 Vimercate, Italy*
[4]*Department of Physics and Nanostructured Interfaces and Surfaces Centre, University of Torino, via Pietro Giuria 1, 10125 Torino, Italy*
[5]*Laboratory of Bio-Inspired and Graphene Nanomechanics, Department of Civil, Environmental and Mechanical Engineering, University of Trento, Via Mesiano 77, 38123 Trento, Italy*
[6]*School of Engineering and Materials Science, Queen Mary University of London, Mile End Road, London E1 4NS, UK*
[7]*Ket Lab, Edoardo Amaldi Foundation, Italian Space Agency, Via del Politecnico snc, 00133 Rome, Italy*
[8]*Centre for Materials and Microsystems, Fondazione Bruno Kessler, via Sommarive 18, 38123 Trento, Italy*
[*]*claudio.castellan@unitn.it*

Abstract: In this work, we analyze the role of strain on a set of silicon racetrack resonators presenting different orientations with respect to the applied strain. The strain induces a variation of the resonance wavelength, caused by the photoelastic variation of the material refractive index as well as by the mechanical deformation of the device. In particular, the mechanical deformation alters both the resonator perimeter and the waveguide cross-section. Finite element simulations taking into account all these effects are presented, providing good agreement with experimental results. By studying the role of the resonator orientation we identify interesting features, such as the tuning of the resonance shift from negative to positive values and the possibility of realizing strain insensitive devices.

OCIS codes: (130.0130) Integrated optics; (130.3060) Infrared; (130.3120) Integrated optics devices; (130.6010) Sensors; (130.6622) Subsystem integration and techniques; (250.5300) Photonic integrated circuits.

References and links

1. K. Harris, A. Elias, and H.-J. Chung, "Flexible electronics under strain: a review of mechanical characterization and durability enhancement strategies," Journal of materials science **51**, 2771–2805 (2016).
2. B. Wang, S. Bao, S. Vinnikova, P. Ghanta, and S. Wang, "Buckling analysis in stretchable electronics," npj Flexible Electronics **1**, 5 (2017).
3. C.-H. Chou, J.-K. Chuang, and F.-C. Chen, "High-performance flexible waveguiding photovoltaics," Scientific reports **3**, 2244 (2013).
4. T. Yokota, P. Zalar, M. Kaltenbrunner, H. Jinno, N. Matsuhisa, H. Kitanosako, Y. Tachibana, W. Yukita, M. Koizumi, and T. Someya, "Ultraflexible organic photonic skin," Science advances **2**, e1501856 (2016).
5. J. Hu, L. Li, H. Lin, P. Zhang, W. Zhou, and Z. Ma, "Flexible integrated photonics: where materials, mechanics and optics meet," Optical Materials Express **3**, 1313–1331 (2013).
6. L. Li, H. Lin, S. Qiao, Y. Zou, S. Danto, K. Richardson, J. D. Musgraves, N. Lu, and J. Hu, "Integrated flexible chalcogenide glass photonic devices," Nature Photonics **8**, 643–649 (2014).
7. Y. Chen, H. Li, and M. Li, "Flexible and tunable silicon photonic circuits on plastic substrates," Scientific reports **2**, 622 (2012).
8. D. Thomson, A. Zilkie, J. E. Bowers, T. Komljenovic, G. T. Reed, L. Vivien, D. Marris-Morini, E. Cassan, L. Virot, J.-M. Fédéli, J.-M. Hartmann, J. H. Schmid, D.-X. Xu, F. Boeuf, P. O'Brien, G. Z. Mashanovich, and M. Nedeljkovic, "Roadmap on silicon photonics," Journal of Optics **18**, 073003 (2016).

#313440 https://doi.org/10.1364/OE.26.004204
Journal © 2018 Received 21 Nov 2017; revised 23 Dec 2017; accepted 24 Dec 2017; published 8 Feb 2018

Optics EXPRESS

9. F. Testa, C. J. Oton, C. Kopp, J.-M. Lee, R. Ortuño, R. Enne, S. Tondini, G. Chiaretti, A. Bianchi, P. Pintus, M.-S. Kim, D. Fowler, J. Á. Ayucar, M. Hofbauer, M. Mancinelli, M. Fournier, G. B. Preve, N. Zecevic, C. L. Manganelli, C. Castellan, G. Parés, O. Lemonnier, F. Gambini, P. Labeye, M. Romagnoli, L. Pavesi, H. Zimmermann, F. D. Pasquale, and S. Stracca, "Design and implementation of an integrated reconfigurable silicon photonics switch matrix in iris project," **22**, 155–168 (2016).
10. W. J. Westerveld, S. M. Leinders, P. M. Muilwijk, J. Pozo, T. C. van den Dool, M. D. Verweij, M. Yousefi, and H. P. Urbach, "Characterization of integrated optical strain sensors based on silicon waveguides," IEEE Journal of Selected Topics in Quantum Electronics **20**, 1–10 (2014).
11. L. Fan, L. T. Varghese, Y. Xuan, J. Wang, B. Niu, and M. Qi, "Direct fabrication of silicon photonic devices on a flexible platform and its application for strain sensing," Optics express **20**, 20564–20575 (2012).
12. S. Leinders, W. Westerveld, J. Pozo, P. Van Neer, B. Snyder, P. O'Brien, H. Urbach, N. de Jong, and M. D. Verweij, "A sensitive optical micro-machined ultrasound sensor (omus) based on a silicon photonic ring resonator on an acoustical membrane," Scientific reports **5**, 14328 (2015).
13. D. Dai, L. Liu, S. Gao, D.-X. Xu, and S. He, "Polarization management for silicon photonic integrated circuits," Laser & Photonics Reviews **7**, 303–328 (2013).
14. M. Borghi, C. Castellan, S. Signorini, A. Trenti, and L. Pavesi, "Nonlinear silicon photonics," Journal of Optics **19**, 093002 (2017).
15. Y. Amemiya, Y. Tanushi, T. Tokunaga, and S. Yokoyama, "Photoelastic effect in silicon ring resonators," Japanese Journal of Applied Physics **47**, 2910 (2008).
16. M. Borghi, M. Mancinelli, F. Merget, J. Witzens, M. Bernard, M. Ghulinyan, G. Pucker, and L. Pavesi, "High-frequency electro-optic measurement of strained silicon racetrack resonators," Optics letters **40**, 5287–5290 (2015).
17. COMSOL Multiphysics® v. 5.2. www.comsol.com. COMSOL AB, Stockholm, Sweden .
18. P. Segall, *Earthquake and volcano deformation* (Princeton University Press, 2010).
19. J. Wortman and R. Evans, "Young's modulus, shear modulus, and poisson's ratio in silicon and germanium," Journal of applied physics **36**, 153–156 (1965).
20. M. A. Hopcroft, W. D. Nix, and T. W. Kenny, "What is the young's modulus of silicon?" Journal of microelectromechanical systems **19**, 229–238 (2010).
21. This estimation is approximated because the spot displacement is determined not only by the sample deflection, but also by the variation of the beam position on mirror M2. This is caused both by the sample movement Δz in the z direction, and by the distance z_0 between the sample surface and the mirror M2. Since $L = 3.73$ m, we have $L \gg z_0 = 0.1$ m. Moreover $\Delta H \gg \Delta z$, being $\Delta H \sim$ cm and $\Delta z < 150$ µm. Thus, the approximation $\delta \sim \Delta H / L$ is valid .
22. W. N. Ye, D.-X. Xu, S. Janz, P. Cheben, M.-J. Picard, B. Lamontagne, and N. G. Tarr, "Birefringence control using stress engineering in silicon-on-insulator (soi) waveguides," Journal of Lightwave Technology **23**, 1308–1318 (2005).
23. R. Edwards, G. Coles, and W. Sharpe, "Comparison of tensile and bulge tests for thin-film silicon nitride," Experimental Mechanics **44**, 49–54 (2004).
24. M. Huang, "Stress effects on the performance of optical waveguides," International Journal of Solids and Structures **40**, 1615–1632 (2003).
25. S. Feng, T. Lei, H. Chen, H. Cai, X. Luo, and A. W. Poon, "Silicon photonics: from a microresonator perspective," Laser & photonics reviews **6**, 145–177 (2012).
26. F. P. Beer, R. Johnston, J. Dewolf, and D. Mazurek, *Mechanics of Materials* (McGraw-Hill, 2006).
27. In the evaluation of the effective refractive index, one should consider that the curved waveguide supports different modes with respect to the straight waveguide. However, since the radius of curvature is much greater than the wavelength and since we are interested in the strain-induced refractive index variation, we performed the simulations considering straight waveguides .

1. Introduction

The role played by strain on the performance of integrated devices is of extreme interest. One of the reasons for this comes from the development of flexible devices. Especially in the field of flexible electronics, many material platforms have been demonstrated, providing high device performance even when subjected to stretching or compression [1, 2]. Flexible optoelectronic devices have also been realized, such as mechanically flexible photovoltaics [3], as well as efficient polymer LEDs and photodetectors [4]. More recently, the integration of photonic structures on flexible platforms has also been realized [5]. This demonstrates the possibility to realize photonic devices such as waveguides, microresonators, add-drop filters and photonic crystals on mechanically flexible supports [6]. Among these realizations, particularly attractive are the ones relying on the transfer of devices realized on the Silicon-On-Insulator (SOI) platform to polymeric flexible substrates [7]. The main reason is that SOI technology, originally developed for electronics, has proved to be an interesting platform for the realization of high-density integrated

Optics EXPRESS

optical structures [8,9], and, thus, also offers interesting features for the realization of complex flexible integrated devices.

In silicon photonics, the role of strain has also been investigated for other applications. For example, silicon-based strain sensors have been realized on standard SOI substrates [10] and on polymeric flexible substrates [11]. Moreover, ultrasound sensors have been realized by a silicon device on a silicon oxide membrane [12]. In addition, straining layers have been deposited on SOI components to control the photoelastic variation of the waveguide refractive index, balancing the geometric birefringence and realizing polarization insensitive devices [13]. Straining layers have also been used to break the centrosymmetric crystalline structure of silicon, introducing second order nonlinear optical effects [14].

In this work, we analyze the role of strain on silicon racetrack resonators, where loading is applied in a controlled way by using a micrometric screw to cause the sample to bend. Extending the study proposed in [10] and [15], we discuss the role played by the resonator orientation with respect to the applied strain, showing that the strain-induced resonance wavelength shift can be tuned from positive to negative values by changing the orientation angle. This offers interesting applications in the field of strain sensors, since different orientations of the resonators on the same sample can provide information on the strain direction. Moreover, choosing the orientation angle to manufacture a strain-insensitive resonator is of extreme interest in the field of flexible photonics, where it is necessary to produce devices insensitive to the applied strain. In this framework, we describe the experimental results, taking into account the different effects responsible for the resonance shift. Our model considers both mechanical deformation of the device, which affects the resonator perimeter and the waveguide cross-section, and the strain-induced refractive index variation, due to the photoelastic effect.

The paper is organized as follows. In Sec. 2 we describe the experimental setup and the analyzed devices, as well as the macroscopic simulation describing the sample bending. In Sec. 3 the experimental results on the strain-induced resonance shift are presented, while in Sec. 4 we describe their simulation. Finally, in Sec. 5 we summarize the results and draw conclusions.

2. The experiment

2.1. Experimental setup and devices

The experimental setup used during this work is sketched in Fig. 1(a). The input and the output channels of the analyzed structures are accessed via edge coupling using tapered lensed fibers, passing in a polarization stage before entering into the input waveguide. The sample is mounted on a screw-equipped sample holder, magnified in Fig. 1(b). The source is a continuous-wave laser, tunable around the wavelength of 1600 nm. The detection is performed using an InGaAs amplified detector coupled to a multimeter. Using the screw, a displacement is applied to the central point of the sample along the direction orthogonal to its main plane (z direction), while the displacement on the sides is inhibited along z, causing the bending of the sample. The point load generates a 2-D strain field in the sample, whose components are principally directed along the longest dimension of the chip. A more complete description of the screw-equipped sample holder can be found in [16].

Figure 1(b) shows our typical test structure. This was designed to assess the strain-induced electro-optic effect in silicon (see more in [16]). The device consists of a racetrack resonator in an add-drop filter configuration designed to work in the Transverse-Magnetic (TM) polarization. It is realized with a 365 nm UV lithography on a 6' SOI wafer, whose cross-section is sketched in Fig. 1(c). Over a 600 µm thick silicon substrate, a 3 µm thick Buried Oxide (BOX) layer forms the lower cladding. All the resonator waveguides have a 243 nm × 400 nm cross-section, guaranteeing the single mode operation at wavelengths around 1600 nm. On the waveguide top, a 140 nm thick silicon nitride layer is conformally deposited via low-pressure chemical vapor deposition. A 900 nm thick plasma-enhanced chemical vapor deposition silica layer forms the

upper cladding. The resonators perimeter is 416 µm, with a straight coupling region length of 12.91 µm, a curvature radius of 15 µm and a 400 nm gap between the resonator and the bus waveguide.

The resonators are fabricated with five different orientations with respect to the silicon crystallographic axes, expressed by the angle α indicated in Fig. 1(b). For $\alpha = 0°$ the resonator longest dimension is oriented along the $[\bar{1}10]$ crystallographic direction. The maximum angle is $\alpha = 90°$, corresponding to a resonator oriented along the [110] direction. Other resonators oriented at angles of $\alpha = 30°$, 45° and 60° are present on the sample.

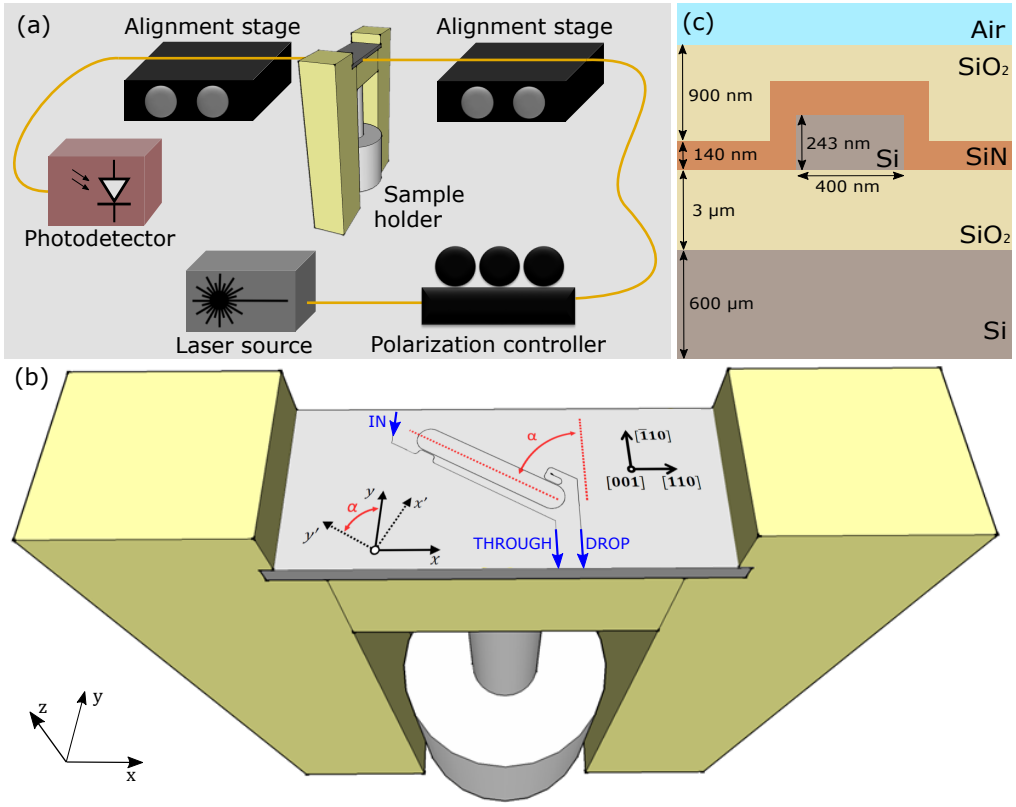

Fig. 1. (a) Sketch of the experimental setup. It is formed by a tunable laser source, a fiber polarization controller, an input-output alignment stage, a screw-equipped sample holder and an InGaAs photodetector. (b) Zoom-in picture of the screw-equipped sample holder. On the sample it is depicted a resonator whose main axis is rotated of an angle α with respect to the y direction. The resonator dimensions are deliberately out of scale. (c) Off-scale picture of the waveguide cross section with nominal dimensions.

2.2. *Description of the local strain: macroscopic simulation of the device*

To compare numerical and experimental results, it is necessary to correctly estimate local strains in the structures due to the sample bending. This estimation is performed with a 3D Finite Element Method (FEM) simulation of the entire sample subjected to a point load using the COMSOL Multiphysics software [17]. The waveguides, BOX and cladding layers are 200 times thinner than the 600 µm thick silicon substrate, so that the latter is mainly responsible for the overall mechanical behavior of the whole sample. As a consequence, in order to reduce the computational burden, the simulation is limited to the silicon substrate. The simulation boundary

Optics EXPRESS

conditions are represented in Fig. 2(a). The effect of the screw is considered as a prescribed displacement along z applied to the center of the sample, while the two supports are modeled by a fixed line constraint and by a prescribed zero z displacement line, which prevents the sample being blocked.

The volumetric strain ε_v is defined as the trace of the strain tensor ε, and it is invariant with respect to rotations of the reference system [18]. In Fig. 2(a) we report the volumetric strain relative to a mechanical displacement of 150 µm applied by the screw. This strain is larger in the center, while approaching the boundaries it decreases and vanishes. The use of the volumetric strain is legitimized by the fact that, from the simulation, it results that the shear components of the stress tensor are at least one order of magnitude smaller than the principal components. The elastic parameters of silicon needed for this simulation, as well as the other material parameters used in this work, are reported in Tab. 1. The stiffness matrix describing the elastic properties of silicon is derived from the elastic parameters corresponding to the crystallographic directions of the sample [19, 20].

The degree of accuracy of the 3D macroscopic simulation is validated via experimental measurements. The sample curvature (as a function of the z-displacement) is experimentally measured as illustrated in Fig. 2(b). Similarly to the method proposed in [15], a HeNe laser impinges on the sample surface and is reflected on a screen. Using the micrometer screw, the sample curvature is modified, causing a movement of the spot position on the screen. The reflected beam is deflected by an angle δ. By using simple geometric considerations, it can be shown that $\delta = 2\theta$, where θ is the rotation of the normal to the sample surface. We determine δ as $\delta \sim \Delta H/L$, being ΔH the spot displacement on the screen and L the distance between the mirror M2 and the screen [21]. In Fig. 2(c) we show the bending angle as a function of the position on the sample surface for three different applied displacement values. The experimental results and the simulation show a good agreement, both varying the position on the sample and the displacement applied by the screw.

Table 1. Material parameters used in this work.

	Silicon	Silicon Oxide	Silicon nitride
Refractive index n (@ 1600 nm)	3.474 [a]	1.443 [a]	1.995 [a]
Young modulus E (GPa)	130 [20][b]	76.7 [22]	255 [23]
Poisson ratio ν	0.28 [20][b]	0.186 [22]	0.23 [23]
Shear modulus G (GPa)	79.6 [20][b]	32.3 [c]	118.6 [c]
Photoelastic coefficient p_{11}	−0.0997 [d]	0.19 [e]	- [f]
Photoelastic coefficient p_{12}	0.0107 [d]	0.27 [e]	- [f]
Photoelastic coefficient p_{44}	−0.051 [g]	−0.04 [h]	- [f]

[a] Measured with ellipsometry technique.
[b] Referred to the reference system with the axes directions [100], [010], [001]. In [19] and [20] the method used to derive the stiffness matrix along arbitrarily directed axes is shown.
[c] Evaluated using $G = E/[2(1+\nu)]$ (valid for isotropic crystals) [24].
[d] Interpolated from measurements taken at λ =1.15 µm and λ =3.39 µm [24].
[e] Interpolated from measurements taken at λ =0.633 µm [24] and λ =1.15 µm [22].
[f] No data in literature. Since silicon nitride forms a thin cladding, no relevant effective index variations can be obtained varying its photoelastic coefficients. Therefore, we use the same values as silica.
[g] Evaluated from [24].
[h] Calculated using the relationship $p_{44} = (p_{11} - p_{12})/2$, that is valid for isotropic crystals [24].

Optics EXPRESS

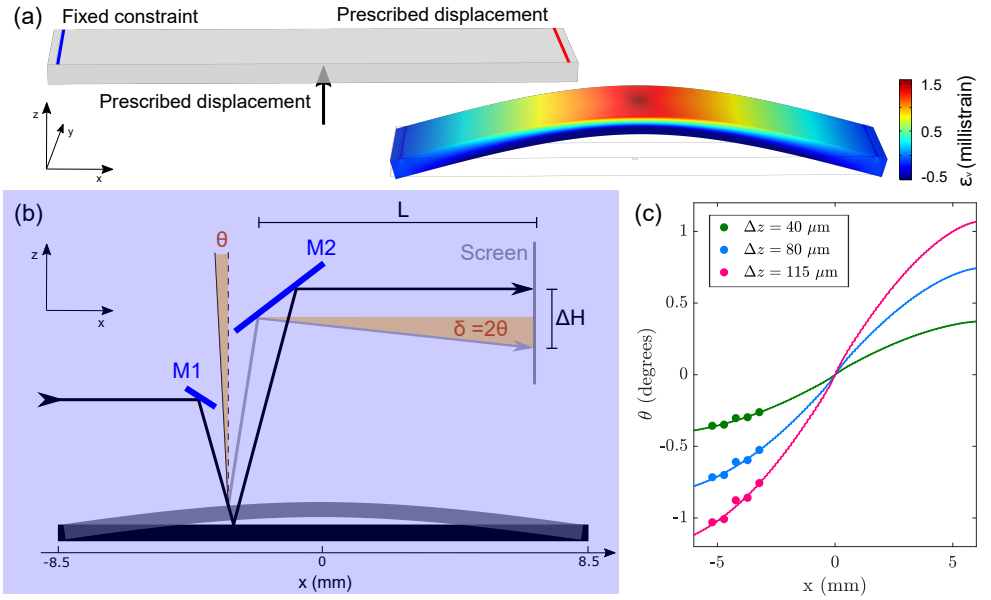

Fig. 2. (a) On the left: 3D simulation boundary conditions for beam bending. The prescribed displacement and the fixed constraint on the top represent the supports, while the arrow describes the screw displacement. On the right: volumetric strain ε_v superimposed in color scale over the beam deformation evaluated applying a displacement of 150 µm to the sample center. Displacements are emphasized by a factor of 10. (b) Setup used to measure the sample curvature. The black line describes the HeNe laser path when the sample is undeformed, while the gray path corresponds to the deformed sample. (c) Rotation of the normal to the surface θ as a function of the position on the sample surface for three different screw displacement Δz values. The experimental data (points) are compared with simulations (straight lines).

3. Experimental results

3.1. *Effect of strain on the resonance wavelength*

The output spectrum recorded on the drop port of an analyzed resonator is shown in Fig. 3(a). The Free Spectral Range (FSR) is about 1.5 nm. The quality factor varies from resonator to resonator in the range 5000 – 10000 due to fabrication variations. In Figs. 3(b)-3(c) we show the transmission spectra of two resonators with different orientation angles α as a function of the displacement Δz applied by the screw in the sample center. In the case of $\alpha = 0°$ the strain induces a blue-shift of the resonance, while it is red-shifted when $\alpha = 90°$. The same fact can be observed from Figs. 3(d)-3(e), where the resonance wavelength dependence on Δz is shown. However, the difference between the two measurements is not only the orientation of the resonator, but also its position on the sample. As it can be seen from Fig. 2(a), even if the displacement applied by the screw at the center of the sample is the same, the strain varies considerably in the sample. Therefore, the local strain level experienced by each resonator can be different. For this reason, the resonance shift must be normalized with respect to the local strain acting on each resonator. The local strain is quantified using the 3D FEM simulation described previously and evaluating the volumetric strain ε_v at the location of the resonator. On the top axes of Figs. 3(d)-3(e) we show the volumetric strains corresponding to the displacements Δz reported on the bottom axes. The slope of the linear fit curve represents the resonance shift per unit strain. Once this normalization is applied, comparable results can be found from identically oriented

Optics EXPRESS

resonators located in different positions on the sample (for example, -0.39 ± 0.09 pm/microstrain and -0.32 ± 0.05 pm/microstrain for two identical resonators oriented with $\alpha = 0°$ situated at about 4.2 mm and 1.9 mm from the center of the sample). We then analyze the resonance shift per unit strain as a function the orientation angle α, reported in Fig. 3(f). The normalized shift increases monotonically with the orientation angle, demonstrating that, tuning the orientation of the resonator on the sample, it is possible to tune the resonance shift from negative to positive values, as well as to design a strain insensitive resonator.

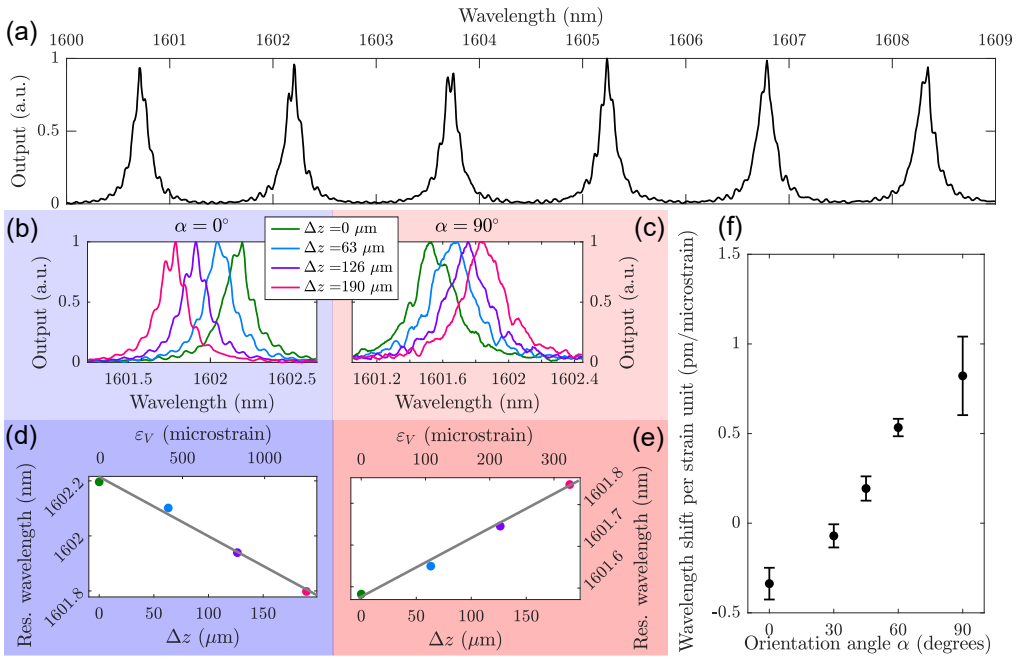

Fig. 3. (a) Drop port spectrum of one analyzed resonator. (b-c) Drop port spectra of two resonators oriented with different angles α. The different colors refer to measurements taken with different screw-applied displacements Δz. (d-e) Dependence on Δz of the resonance wavelength evaluated from a Lorentian fit of the spectra. The top axes report the corresponding volumetric strain evaluated from the 3D macroscopic simulation. The gray lines are linear fits of the experimental points. (f) Resonance shift per strain unit for resonators oriented with different angles α. Errorbars represent 95% confidence bounds resulting from the linear fits.

3.2. *Role of the waveguide deformation and determination of the waveguide width*

In Fig. 4(a) we show the wavelength dependence of the group index n_g for one analyzed resonator. The experimental values are evaluated from the experimental FSR using $n_g = \lambda_m^2 P^{-1} \mathrm{FSR}^{-1}$, being λ_m the $m-$th resonant wavelength and P the resonator perimeter [25]. The group index is evaluated for different strain levels applied by the screw. The group index variation induced by the applied strain is below the measurement error level, revealing that in this way we are not able to detect any deformation of the waveguide cross section caused by strain. A similar observation derives from Fig. 4(b), where the experimental wavelength dependence of the quality factor is reported. Any variation of the quality factor caused by strain (such as the variation of the gap between the resonator and the bus waveguide) is below the experimental error.

The comparison between the experimental group index and the simulation can provide an estimation of the actual dimensions of the analyzed resonator waveguide. Fabrication uncertainties affect mainly the waveguide width rather than the height. Therefore, we set the waveguide height

Optics EXPRESS

to its nominal value of 243 nm (evaluated from interferometric measurements) and we evaluate the group index dependence on the waveguide width. This is calculated with a 2D mode solver from the effective refractive index dispersion, and is shown in black in Fig. 4(c). The blue line represents the experimental value of the group index, evaluated from the data shown in Fig. 4(a). From the intercept between the experimental and the theoretical group index we can estimate that the actual waveguide width of the resonator is 391 ± 7 nm, slightly smaller than the nominal value of 400 nm. Any variation of the waveguide width caused by strain is below the error of this estimation. In Fig. 4(d) we show the waveguide width evaluated from the experimental group index for all the resonators analyzed in this work, providing a mean width of 384 ± 2 nm.

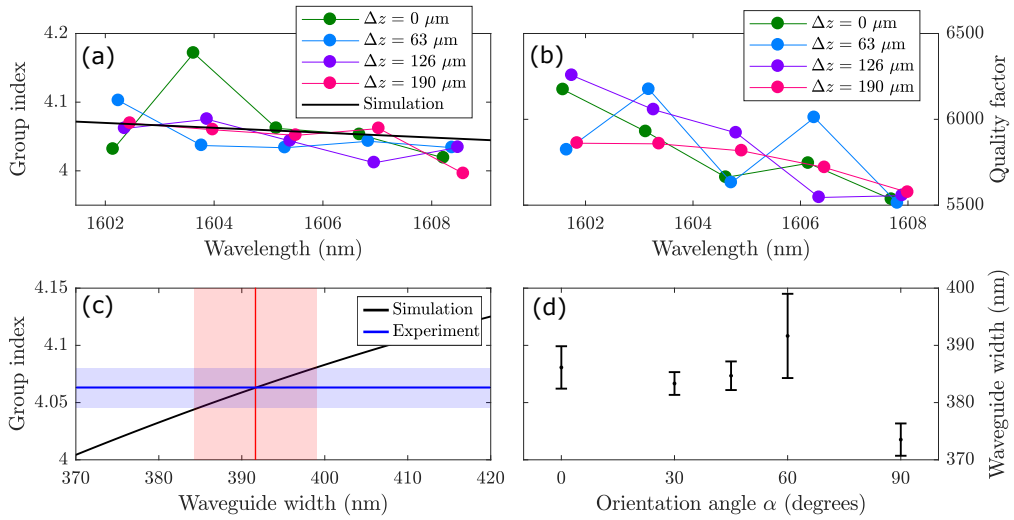

Fig. 4. (a) Wavelength dependence of the group index of the resonator with an orientation angle $\alpha = 60°$. The experimental value is evaluated from the FSR, while the simulated result derives from a FEM simulation of a waveguide with a cross section of 390 nm × 243 nm. (b) Wavelength dependence of the quality factor of the same resonator. (c) Comparison between the simulated dependence of the group index on the waveguide width (black) and the experimental value (blue), from which the actual width of the waveguide is determined (red). The light colors represent the errorbars. (d) Waveguide width evaluated from the experimental group index for the resonators analyzed in this work.

4. Modeling the strain-induced resonance shift

In all the simulations we use the mean experimental group index value ($n_g = 4.08$) and we consider the mean waveguide width determined in Sec. 3.2 ($w = 384$ nm).

4.1. Theoretical model

Here, we generalize the model proposed in [10] by taking into account the role of strain not only on the straight parts of the racetrack resonator, but also on the curved ones. The starting point is the racetrack resonator resonance condition:

$$m\lambda_m = 2Ln_s + 2\pi R\bar{n}_c, \tag{1}$$

where m is an integer number, λ_m the m-th resonant wavelength, n_s the effective refractive index of the straight waveguide, L the length of the straight part of the resonator and R the resonator radius (as it is sketched in Fig. 5(a)). The quantity $\bar{n}_c$ is the mean effective refractive index in the

Optics EXPRESS

curved section, which is related to the effective refractive index $n_c(\gamma)$ at a generic angle γ on the curve according to the relationship:

$$\overline{n}_c = \frac{1}{\pi}\int_0^{\pi} n_c(\gamma)\,\mathrm{d}\gamma\,. \tag{2}$$

When dealing with photoelasticity this dependence is important because the refractive index components in the different directions depend on the strain value in the different directions. If the resonator is subjected to an external strain, the general resonance condition (1) can be derived with respect to the applied volumetric strain ε_v. Eq. (1) can be used again to replace the value of m. In doing this, we must consider that the effective refractive indices depend both on the local strain and on wavelength, and so we must write:

$$\frac{\mathrm{d}}{\mathrm{d}\varepsilon_v} n_s(\varepsilon_v,\lambda) = \frac{\partial n_s}{\partial \varepsilon_v} + \frac{\partial n_s}{\partial \lambda}\frac{\partial \lambda}{\partial \varepsilon_v} \qquad \frac{\mathrm{d}}{\mathrm{d}\varepsilon_v} \overline{n}_c(\varepsilon_v,\lambda) = \frac{\partial \overline{n}_c}{\partial \varepsilon_v} + \frac{\partial \overline{n}_c}{\partial \lambda}\frac{\partial \lambda}{\partial \varepsilon_v}. \tag{3}$$

Moreover, we need to consider that the strain has a dual effect on the effective refractive index: on the one hand it modifies the material refractive index due to the photoelastic effect, on the other hand it deforms the waveguide cross-section. These two contributions are separated as follows:

$$\frac{\partial n_s}{\partial \varepsilon_v} = \left.\frac{\partial n_s}{\partial \varepsilon_v}\right|_{\mathrm{ph}} + \left.\frac{\partial n_s}{\partial \varepsilon_v}\right|_{\mathrm{def}} \qquad \frac{\partial \overline{n}_c}{\partial \varepsilon_v} = \left.\frac{\partial \overline{n}_c}{\partial \varepsilon_v}\right|_{\mathrm{ph}} + \left.\frac{\partial \overline{n}_c}{\partial \varepsilon_v}\right|_{\mathrm{def}}. \tag{4}$$

Finally, the following equation is derived:

$$\frac{\partial \lambda_m}{\partial \varepsilon_v} = \frac{\partial \lambda_m^{\mathrm{per}}}{\partial \varepsilon_v} + \frac{\partial \lambda_m^{\mathrm{ph}}}{\partial \varepsilon_v} + \frac{\partial \lambda_m^{\mathrm{def}}}{\partial \varepsilon_v}, \tag{5}$$

where we introduced the resonance shift due to the perimeter variation $\partial\lambda_m^{\mathrm{per}}/\partial\varepsilon_v$, the resonance shift due to the photoelastic-induced refractive index variation $\partial\lambda_m^{\mathrm{ph}}/\partial\varepsilon_v$ and the resonance shift due to the waveguide deformation $\partial\lambda_m^{\mathrm{def}}/\partial\varepsilon_v$. These quantities are given by:

$$\frac{\partial \lambda_m^{\mathrm{per}}}{\partial \varepsilon_v} = \frac{\lambda_m n_s}{P n_g}\frac{\partial P}{\partial \varepsilon_v}, \tag{6a}$$

$$\frac{\partial \lambda_m^{\mathrm{ph}}}{\partial \varepsilon_v} = \frac{\lambda_m}{P n_g}\left(2L\left.\frac{\partial n_s}{\partial \varepsilon_v}\right|_{\mathrm{ph}} + 2\pi R\left.\frac{\partial \overline{n}_c}{\partial \varepsilon_v}\right|_{\mathrm{ph}}\right), \tag{6b}$$

$$\frac{\partial \lambda_m^{\mathrm{def}}}{\partial \varepsilon_v} = \frac{\lambda_m}{P n_g}\left(2L\left.\frac{\partial n_s}{\partial \varepsilon_v}\right|_{\mathrm{def}} + 2\pi R\left.\frac{\partial \overline{n}_c}{\partial \varepsilon_v}\right|_{\mathrm{def}}\right). \tag{6c}$$

We introduced here the racetrack resonator perimeter $P = 2L + 2\pi R$ and the straight waveguide group index $n_g = n_s - \lambda(\partial n_s/\partial\lambda)$. Deriving this, we considered the curved group index equal to the straight group index, based on the fact that the radii of the resonators analyzed in this work are much larger than wavelength. For the same reason, we considered also the curved effective refractive index the same of the straight waveguide ($\overline{n}_c = n_s$). On the other hand, the applied strain can act differently on the straight and on the curved waveguides, and therefore we kept $\partial n_s/\partial\varepsilon_v \neq \partial\overline{n}_c/\partial\varepsilon_v$.

The following sections are dedicated to the separate study of these contributions. Finally, the global contribution will be compared to the experimental measurements.

Optics EXPRESS

4.2. Contribution of the perimeter variation

Equation (6a) shows that the evaluation of the resonance wavelength shift induced by the resonator perimeter variation $\partial\lambda_m^{\mathrm{per}}/\partial\varepsilon_v$ requires the knowledge of two quantities. The first one is the effective index n_s, and is evaluated by a 2D mode solver. The second one, the perimeter dependence on the local volumetric strain $\partial P/\partial\varepsilon_v$, is calculated from the macroscopic 3D simulation of the sample deformation described in Sec. 2.2.

The local strain experienced by each resonator is evaluated from the macroscopic simulation of the sample. For a generic resonator oriented at an angle α, the strain tensor components along the main resonator axes ($\varepsilon_{x'x'}$ and $\varepsilon_{y'y'}$) are evaluated from the strain components along the original axes (ε_{xx} and ε_{yy}) and from the shear strain element (ε_{xy}) using [26]:

$$\varepsilon_{x'x'} = \varepsilon_{xx}\cos^2\alpha + \varepsilon_{yy}\sin^2\alpha + 2\varepsilon_{xy}\sin\alpha\cos\alpha, \tag{7a}$$

$$\varepsilon_{y'y'} = \varepsilon_{xx}\sin^2\alpha + \varepsilon_{yy}\cos^2\alpha - 2\varepsilon_{xy}\sin\alpha\cos\alpha. \tag{7b}$$

As it is sketched in Fig. 5(a), the new length of the straight part of the resonator L' is:

$$L' = L(1 + \varepsilon_{y'y'}), \tag{8}$$

while the resonator curved part assumes an ellipsoidal shape whose semi-axes R_a and R_b are:

$$R_a = R(1 + \varepsilon_{y'y'}) \qquad R_b = R(1 + \varepsilon_{x'x'}). \tag{9}$$

The new perimeter P' of the resonator is then:

$$P' = 2L' + 2\pi\sqrt{\frac{R_a^2 + R_b^2}{2}}. \tag{10}$$

Equations (8) and (9) show that the local volumetric strain is the relevant parameter to calculate the perimeter variation, it gathers by itself alone the resonator position on the sample and the global strain induced by the screw. As a consequence, also the results shown in the following section regarding the refractive index variation effects are independent from the position on the macroscopic simulation surface as long as the resonance shift is normalized on the local volumetric strain. This fact agrees with the experimental observation that the resonance shift per strain unit does not depend on the location on the sample but only on the orientation angle.

In Fig. 5(b) we show the simulated perimeter variation dependence on the local volumetric strain ε_V for different resonator orientations α. Increasing the strain, the perimeter increases. This effect is maximized when the orientation of the resonator main axis approaches the main axis of the sample ($\alpha = 90°$), where the elongation effect on the straight part of the resonator is maximum. In Fig. 5(c) we show the perimeter variation per unit of volumetric strain ($\partial P/\partial\varepsilon_v$) as a function of the resonator orientation angle α. This quantity is calculated from a linear fit of the results shown in Fig. 5(b). Eventually, the resonance shift due to the perimeter variation $\partial\lambda_m^{\mathrm{per}}/\partial\varepsilon_v$ is calculated from Eq. (6a) and is shown on the right axis of Fig. 5(c). A positive variation of the volumetric strain ε_V induces a red-shift of the resonance, and the magnitude of this shift increases as the resonator orientation approaches the main direction of the sample.

4.3. Contribution of the effective refractive index variation

The evaluation of the strain effect on the effective refractive index requires the knowledge of the stress/strain distribution inside the resonator waveguides. Then the photoelastic matrix is used to connect the stress map to the stress-induced refractive index variation map, from which the new effective refractive index of the propagating mode is calculated using the usual mode solver. Similarly, the waveguide deformation is determined from the strain distribution inside the waveguide, determining then the effective refractive index in the deformed waveguide.

Optics EXPRESS

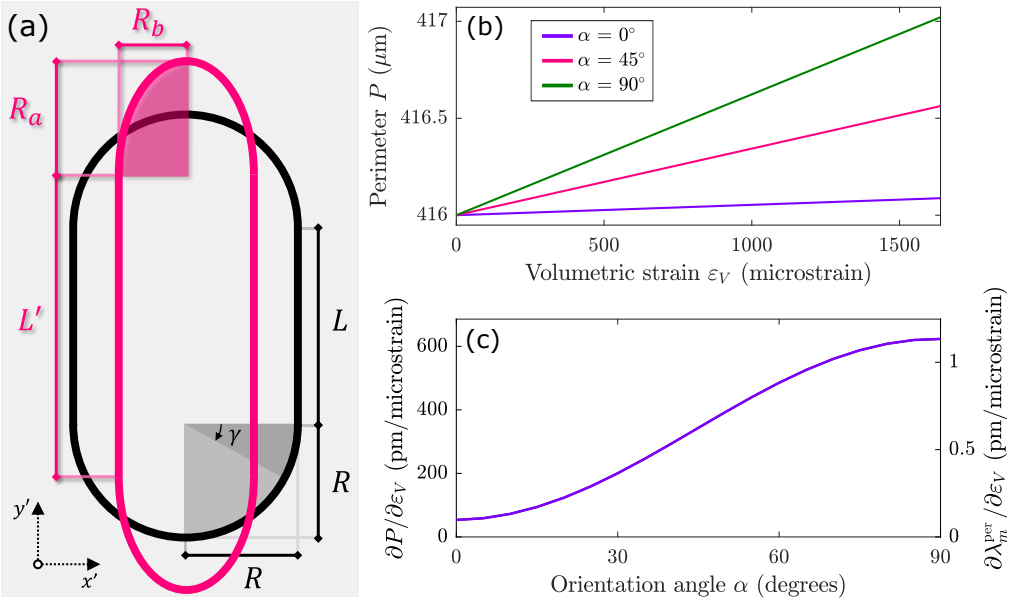

Fig. 5. (a) Out of scale model showing the effect of strain on the resonator. The unstrained resonator shape (in black) is modified by strain into the magenta shape. (b) Simulated dependence of the resonator perimeter P on the applied volumetric strain ε_V for different resonator orientation angles. (c) Dependence of the perimeter variation per unit of volumetric strain on the orientation angle. The corresponding resonance shift is shown on the right axis.

4.3.1. Evaluation of the strain distribution inside the waveguide

Since there are three orders of magnitude between the size of the waveguide and that of the sample, it is impossible to use the global 3D simulation presented in Sec. 2.2 to determine the strain distribution inside the waveguide. Therefore, only a limited area sketched in Fig. 6(a), constituted by the oxide substrate, the waveguide and the cladding layers is modeled. Nevertheless, the global strain induced by the screw is taken from the macroscopic simulation, properly rotated in the $xy-$plane using Eq. (7) and applied in terms of prescribed displacements at the bottom of the oxide substrate.

The size of the reduced simulation is properly chosen to avoid unwanted boundary effects in the waveguide core. Apart from silicon, all the involved materials are amorphous, and so their elastic properties do not depend on the orientation of the analyzed structures. On the contrary, for silicon it is important to consider the crystallographic direction along which the structure is grown, and its stiffness matrix must be rotated according to the crystallographic direction along which the waveguide is directed [19, 20]. As an example, in Fig. 6(b) we report the normal x' component of the stress tensor in the waveguide cross-section plane. The simulation refers to the resonator oriented at $\alpha = 0°$ when a displacement $\Delta z = 150\,\mu$m is applied.

This method can also be used to evaluate the strain distribution in the resonator curved section. In this case, the strain distribution in the waveguide curve at an angle γ is evaluated applying a rotation of $\alpha + \gamma$ to both the boundary conditions and the silicon stiffness matrix. In principle, the evaluation of this quantity should consider that the waveguide is curved. However, since the radius of curvature is large (15 µm), the strain distribution in the waveguide is well approximated without accounting for curvature.

In this framework, one should also take into account the residual stresses introduced during the deposition of the cladding materials, which must be considered in the simulation as initial stress

conditions. However, in our case we are interested in the study of the strain-induced refractive index variation, which is a differential quantity related to the strain variation rather than to the absolute strain inside the waveguide. Therefore, since we are using a linear model, the presence of residual stresses can be omitted. To verify the validity of the approximation, all the simulations described in the following have been performed with and without considering residual stresses, finding negligible differences in terms of the predicted resonance wavelength shift.

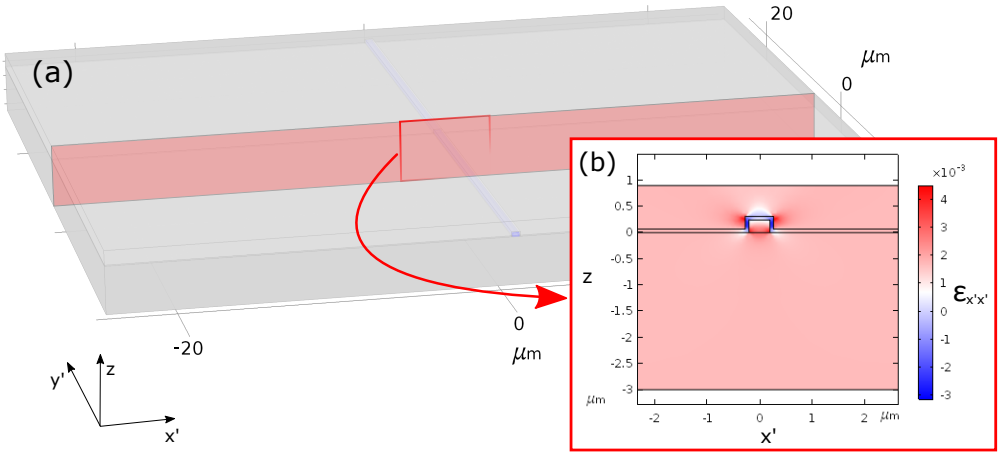

Fig. 6. (a) Simulation domain of the local 3D strain simulation of the waveguide. (b) Color scale strain distribution in the waveguide cross-section in the simulation domain center.

4.3.2. Photoelastic variation of the effective refractive index

Once the stress distribution inside the waveguide cross-section is evaluated as described in the previous point, the photoelastic matrix can be used to calculate the strain-induced refractive index variation [24]. It is worth noting that this matrix also needs to be rotated according to silicon crystallographic directions. Once the new refractive indexes of all the involved materials are evaluated, the new effective refractive index is evaluated using a FEM mode solver [22]. While doing this in the straight part of the resonator is straightforward, in the evaluation of the curved index $n_c(\gamma)$ one should consider that the cross-section plane in the curve rotates with an angle described point-by-point by γ. However, as a further approximation, we assume that the effective refractive index varies continuously from the straight index n_s to the effective refractive index evaluated in the halfway point of the curved section $n_\perp$ (corresponding to the angle $\gamma = 90°$) [27]. Thus, our estimation of $n_c(\gamma)$ is:

$$n_c(\gamma) = n_s \cos^2(\gamma) + n_\perp \sin^2(\gamma), \tag{11}$$

from which the mean index in the curved $\overline{n}_c$ is calculated using Eq. (2). Through this approach, for a given resonator orientation and for a given applied strain, the effective refractive index is evaluated in the straight part (n_s) and in the halfway point of the curve ($n_\perp$). In Fig. 7(a) we show the simulated effective refractive index variation per strain unit for both n_s and $\overline{n}_c$. Eq. (6b) allows then to evaluate the photoelastic contribution to the resonance wavelength shift $\partial\lambda_m^{\mathrm{ph}}/\partial\varepsilon_v$, that is shown in Fig. 7(b). This plot shows that the shift increases with the resonator orientation angle, moving from negative to positive values.

4.3.3. Contribution of the waveguide deformation to the effective refractive index

The deformation-induced effective refractive index variation is evaluated using the same approach proposed for the photoelastic effect. For the straight part of the resonator, the new effective

Optics EXPRESS

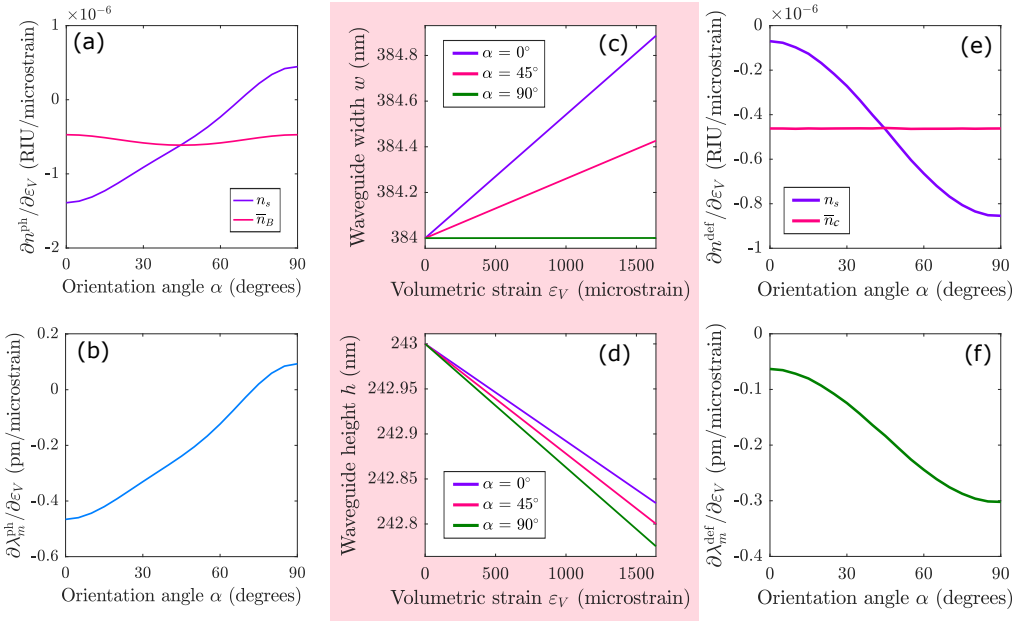

Fig. 7. (a) Photoelastic variation of the effective refractive index in the straight and in the curved part of the resonator as a function of the resonator orientation. (b) Photoelastic contribution to the resonance wavelength shift. (c-d) Waveguide width and height in the straight part of the resonator as a function of the applied strain and for different orientations. (e) Waveguide deformation effect on the effective refractive index in the straight and in the curved part of the resonator. (f) Contribution of the waveguide deformation to the resonance wavelength shift.

refractive index is determined once that the deformed waveguide cross-section in the straight part is known. Similarly, once the effective refractive index of the deformed waveguide is evaluated in the middle of the curve, the index at a generic angle γ of the curve is calculated using Eq. (11). Both in the straight part and in the middle of the curve, the waveguide deformation is estimated calculating the mean strain values in the waveguide cross-section directions ($\overline{\varepsilon}_{x'x'}$ and $\overline{\varepsilon}_{zz}$) from the 3D simulation of the waveguide. Assuming that the deformed waveguide again maintains its rectangular cross-section, its new height h' and width w' are related to the unstrained parameters h and w by:

$$h' = h(1 + \overline{\varepsilon}_{zz}) \qquad w' = w(1 + \overline{\varepsilon}_{x'x'}). \tag{12}$$

The dependence on the applied volumetric strain of the waveguide height and width in the straight part of the resonator are shown in Fig. 7(c-d). First, we notice that the waveguide width variation is below the typical errorbar of the estimation given in Sec. 3.2. Moreover, for all the resonator orientations, the waveguide height decreases as the volumetric strain increases, showing a larger effect on the resonators oriented along the main direction of the sample ($\alpha = 90°$). On the other hand, an increase of the volumetric strain causes an increase of the waveguide width, whose magnitude progressively reduces from $\alpha = 0°$ to $\alpha = 90°$. Due to this fact, for the resonator oriented at $\alpha = 0°$ the effect of the height reduction is balanced by the increase of the waveguide width, determining a small effective refractive index variation. On the contrary, the waveguide of the resonator oriented at $\alpha = 90°$ is mainly influenced by the height reduction and by only a small width increase, thus displaying a larger effective refractive index variation. This fact can be observed in Fig. 7(e), where the effective refractive index variation caused by the waveguide deformation is shown. In Fig. 7(f) we show the waveguide deformation contribution to the

Optics EXPRESS

resonance wavelength shift $\partial\lambda_m^{\mathrm{def}}/\partial\varepsilon_v$ evaluated using Eq. (6c).

4.4. Comparison with experiments

Figure 8 shows, as a function of the resonator orientation angle, the three contributions to the resonance shift calculated so far: the one from the perimeter variation, the photoelastic effect and the transverse waveguide deformation. Moreover, according to Eq. (5), the sum of these contributions gives the global resonance wavelength shift resulting from a strain applied to the microresonator. Finally, the experimental points from Fig. 3(f) are added. A good agreement is observed, which legitimizes the approximations made in the model.

For small angles, i.e. when the resonator is perpendicular to the direction of the elongation imposed to the sample, the photoelastic effect is the main contribution. The contributions related to the mechanical deformation of the device, such as the one due to the perimeter variation and the one related to the transverse waveguide deformation, are smaller and balance themselves. On the contrary, for large angles, the perimeter variation plays the dominant role. Besides, this contribution is the one that has the largest variation amplitude with respect to the sample orientation, roughly twice the ones of the two others.

Varying the orientation angle, the global resonance wavelength shift changes sign, passing from a negative to a positive shift. The angle where the shift approaches 0 is at about 34.5°, where all the contributions balance giving rise to a strain insensitive resonator.

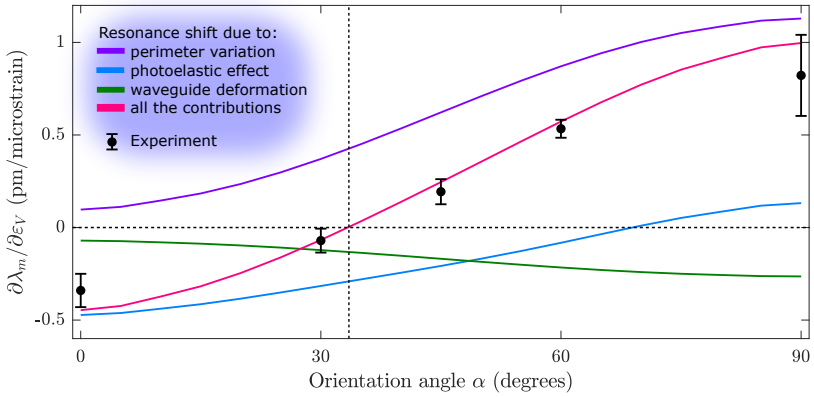

Fig. 8. Resonance shift as a function of the resonator orientation angle. The experimental data are shown as black dots. The simulated contributions to the resonance shift of perimeter variation (blue), photoelastic effect (light blue) and waveguide deformation (green) add up providing the total simulated resonance shift (magenta). The dashed lines show the orientation angle corresponding to the strain insensitive resonator.

5. Conclusion

In this work, we analyzed the role of strain on a set of elongated SOI racetrack resonators presenting different orientation angles. We proposed a 3D simulation of the whole deformed chip, through which the resonance wavelength shift was normalized to the local strain value experienced by each resonator. Moreover, we proposed an analysis featuring a macroscopic simulation model able to take into account all the effects causing the shift of the resonance wavelength. The strain-induced perimeter variation was considered, as well as the strain-induced variation of the material refractive index and the deformation of the waveguide cross-section. The simulated results are in good agreement with the experimental resonance shifts, which vary from positive to negative values when changing the resonator orientation angle. The possibility

Optics EXPRESS

of tuning the resonance shift value by changing the resonator orientation offers interesting applications in the field of strain sensors, since the presence of many resonators with different orientations on the same sample can provide information on the strain direction. Moreover, the resonator orientation angle can be tuned in order to realize strain-insensitive resonators, offering interesting applications in the field of flexible photonics.

Funding

Provincia Autonoma di Trento; MIUR (PRIN 2015KEZNYM); H2020 (732344, 696656).

Acknowledgments

The authors affiliated with the Nanoscience Laboratory are supported by the Siquro project (Bando grandi progetti, Provincia Autonoma di Trento, 2012) and by the NEMO project (PRIN 2015KEZNYM supported by MIUR). F.B. is supported by H2020 FET Proactive "Neurofibres". N.M.P. is supported by the European Commission H2020 under the Graphene Flagship Core 1 No. 696656 (WP14 "Polymer composites") and FET Proactive "Neurofibres".

The authors M.B., M.G. and G.P. acknowledge the support of the staff of the Micro Nano Facility during device fabrication.